Accepted Manuscript

The influence of liner material on the dynamic response of the finite steel target subjected to high velocity impact by explosively formed projectile

Jianfeng Liu , Yuan Long , Chong Ji , Mingshou Zhong , Qiang Liu

Please cite this article as: Jianfeng Liu , Yuan Long , Chong Ji , Mingshou Zhong , Qiang Liu , The influence of liner material on the dynamic response of the finite steel target subjected to high velocity impact by explosively formed projectile, *International Journal of Impact Engineering* (2017), doi: 10.1016/j.ijimpeng.2017.07.002

The influence of liner material on the dynamic response of the finite steel target subjected to high velocity impact by explosively formed projectile

Jianfeng Liu[1], Yuan Long[1], Chong Ji[1,2], Mingshou Zhong[1], Qiang Liu[1]

[1]*College of Field Engineering, PLA University of Science and Technology, Nanjing Jiangsu 210007, China*

[2]*State key Laboratory of Explosion Science and Technology, Beijing Institute of technology,Beijing100081,China*

ABSTRACT: Subjected to high velocity impact(collision pressure over 30GPa) of copper and iron liner EFP, the finite steel targets experience the failure modes of plug and spall. Dynamic deformation and microstructure evolution of the finite steel targets are investigated in detail through ANSYS/LS-DYNA software and experiment methods including optical, scanning and transmission electron microscopy. Morphology analysis of fracture surfaces indicates that the copper EFP remainder plated to the crater wall shows extremely plastic deformation which consists of elongated parabolic dimples on the crater wall and the mild carbon steel target exhibits excellent brittle features that material fails mainly along the cleavage facets on the rear surface of target. The whole part of copper EFP remainder and partial material of steel target undergoes completely dynamic recrystallization, which displays an extreme plastic flow. The thickness of irregular DRX zone(30.4μm) formed by the interaction between iron EFP and steel target is wider than the thickness of DRX zone(21.3μm) formed by the penetration of copper EFP. Numerical simulation results indicate that the highest plastic strains at the crater wall can reach about 2 which can fully accommodate the grains deformation of steel target during the dynamic recrystallization process at strain rates of the order of 10^4 s^{-1}, and the average size of the refined DRX grains significantly decreases from 53.17 μm to approximately 200 nm. The refined grains in the DRX zone and elongated grains in the SPD zone distribute along EFP impact direction. Irreversible plastic deformation of grains extending from the crater wall to the matrix of steel target is consistent with the microhardness changes.

Keywords: Liner material; Terminal effects; Numerical simulation; Fracture morphology; Microstructure evolution

1. Introduction

Explosively formed projectile (EFP) is a kind of shaped charge structure that demonstrates high penetration ability in weapon engineering [1,2]. A complete EFP warhead consists of a metallic liner, high-energy explosive (HE), case, a slotted ring or sleeve and a detonator[3]. After detonation, the EFP warhead liner undergoes extreme, yet controlled, plastic deformation driven by explosive[4]. As the appearance of projectile is stable, the velocity of EFP is about 1500-2500m/s in a long rod-shaped, with a high kinetic energy[5]. The various failure modes of target are caused by the kinetic energy of the projectiles, including perforation, plug, and spall[6-8]. When the projectile geometry and material changing, the target responds accordingly by accommodating deeper penetration for larger aspect ratio(the dimensionless ratio of length and diameter) of the projectile, and higher projectile densities relative to the target density(ρ_P/ρ_T)[9]. For small projectiles impacting semi-infinite or infinite targets(with thickness orders of magnitude greater than the projectile dimensions) at high velocity, the penetration into the target may be only a small crater which scales with the projectile diameter. However, the projectile is fragmented or eroded, leaving some fractional mass in the cratered target [10,11]. As the projectile dimensions and the thicknesses of target are in the same order of magnitude, the projectile striking a target effectively distributes its initial kinetic energy between itself and the target, as well as the plug from the rear of a target with finite thickness [12-14]. During high velocity impact by EFP, dynamic responses and damage modes of different targets are varied from each other according to the loads they are subjected to.

As a key component of EFP warhead, the liner experiences essentially plastic strains up to 300%, at strain rates of the order of 10^4 s^{-1}[15]. Therefore, the properties of the liner are important during the dynamic EFP formation process. The eventual effectiveness of the liner as a projectile is attributed to its high density, high ductility, high strength and sufficiently high melting temperature which prevent melting caused by adiabatic heating. Tantalum, copper, iron, molybdenum and tantalum-tungsten alloys have been used in EFP applications. A detailed microstructural analysis on Ta EFPs by Murr et al.[16,17] reveals that dynamic recovery (DRV) is a predominant mechanism influencing the EFP formation. Pappu[18]

designs a "soft-catch" device for the safe recovery of EFP to obtain an Armco iron EFP and an oxygen-free high-conductivity (OFHC) copper EFP. They also use several analytical tools and microanalysis approaches to identify and resolve the microstructural and microchemical issues in materials. As a chemical energy projectile which is one of the most common weapon used to defeat the armor, the penetration mechanism and microstructural evolution of the target subjected to high velocity impact by EFP are obviously different from the traditional kinetic energy projectile[19]. However, reports on microstructural features of high velocity impact crater in target penetrated by EFP are limited and inconsistent. The dynamic response process of target is still far from understand completely and there are still many basic issues that should to be investigated further. Besides, study on the microcosmic damage mechanism influenced by the liner material is beneficial to take advantage of the inherent properties of the liner itself (such as density, ductility and strength). Choosing the corresponding liner material according to the characteristics of different targets, terminal effects of EFP warhead can also be significantly improved.

This paper concentrates on the influence of liner materials on the dynamic deformation and microstructure evolution of the finite steel target subjected to high velocity impact by EFP. Formation and penetration properties of EFP are investigated through ANSYS/LS-DYNA software and experiment methods including optical, scanning and transmission electron microscopy. Theoretical calculation results related to collision pressure and numerical simulation analysis about plastic strain changes of steel target are also presented in detail. Finally, conclusions are drawn based on the results obtained.

2. Experimental procedure

The EFP warhead contains of polyvinyl chloride (PVC) casing, liner, explosive and the point initiator. The structures of the EFP warhead and liners are shown in Fig.1. The casing is machined onto a lathe and has a threaded end that holds the rear of the charge. The high explosive 8701 with a nominal density of 1.71 g/cm^3 and a detonation velocity of 8315 m/s is used. This explosive is initiated by a pressed PBX 9407 explosive precision booster and an 8# detonator. The diameter of the liner is 56 mm and its shape is a combination of an arc and a cone. The liner is subjected to stress relief annealing prior to explosive filling. In order to study the influence of liner material on the terminal effects of EFP warhead, two kinds of EFP warhead are designed with copper and iron liners. The copper liner with tensile strength of 35-45% and ductility of 45% [20] weighs 69.4g. The iron liner with tensile strength of 25-40% and ductility of 38%[20] weighs 60.6g. The copper or iron liner is shocked at approximately 30 GPa or higher[21] when the explosive is initiated.
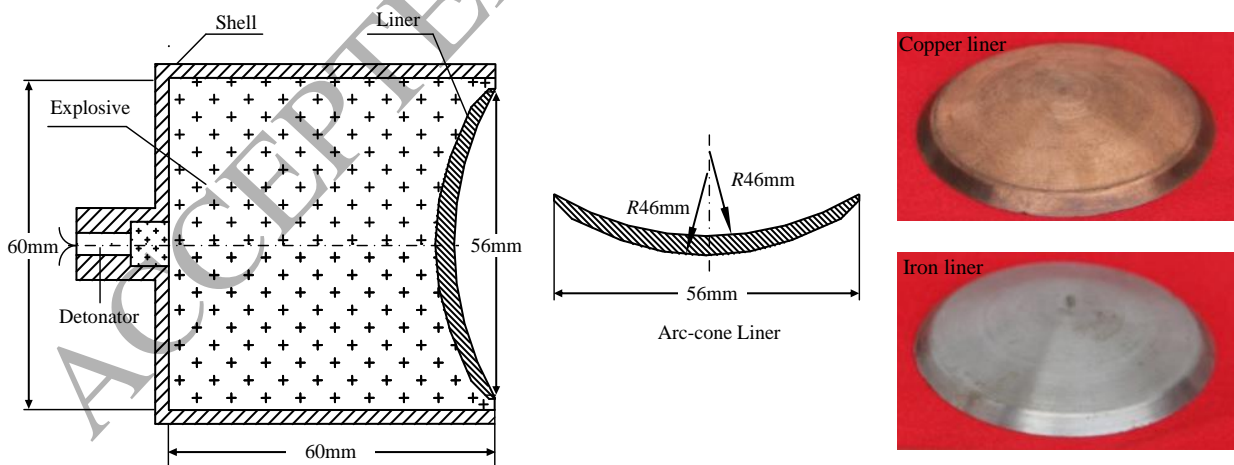

Fig.1. Structure of the EFP warhead and the liners.

Fig.2 illustrates the schematic of the experimental device and measuring equipment. Once initiated, the damage of a mild carbon steel target is caused by the kinetic energy of EFP. The average velocity of EFP can be measured as the projectile passes through two layers of velocity measurement screens. In our experiment, the velocity of copper EFP is 1489 m/s and the velocity of iron EFP is 1632.73 m/s.
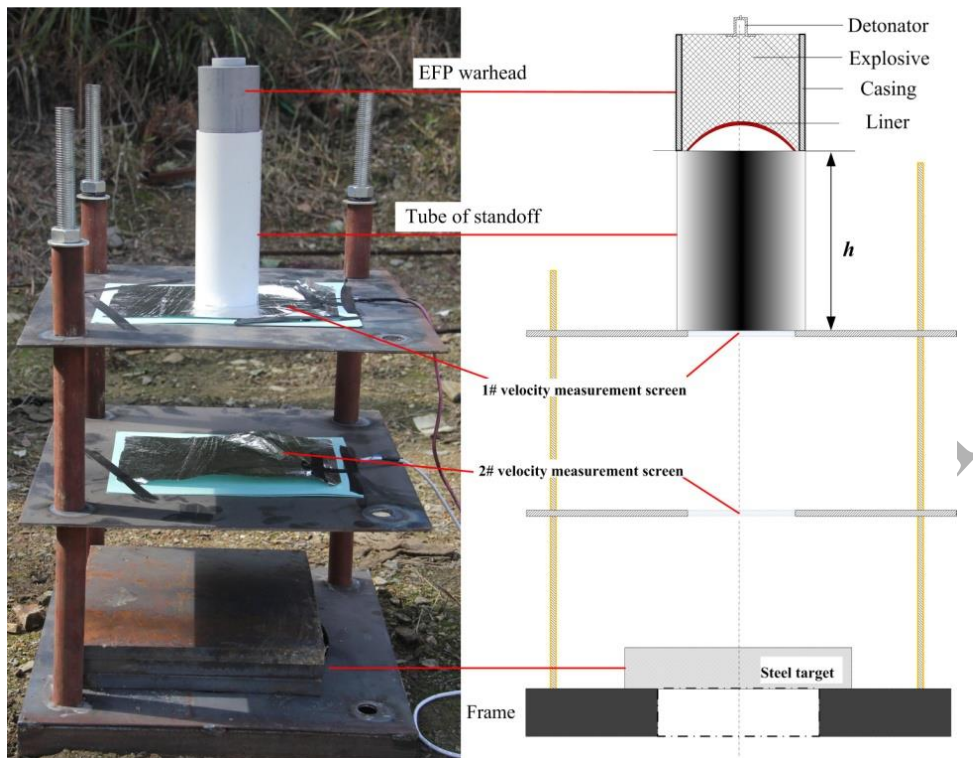
Fig.2. Experimental setup of EFP terminal effects.

3. Numerical modeling and formation process of EFP

3.1 Establishment of the simulation model

Numerical simulation is carried out using three-dimensional (3D) dynamic finite element program of ANSYS/LS-DYNA in order to study the formation and penetration properties of EFP. The simulation model of the EFP warhead and steel target are presented in Fig.3. Due to symmetry, modeling 1/2 of the geometry is necessary to simplify the analysis and reduce the computational cost.
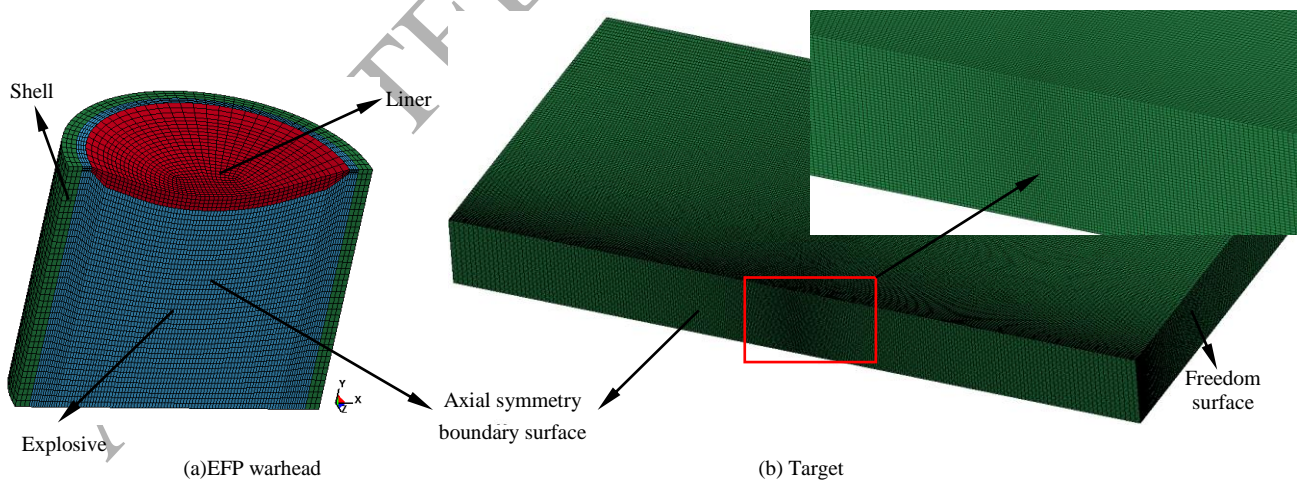

(a)EFP warhead   (b) Target

Fig.3. Simulation model of EFP warhead and steel target (1/2 model).

The explosive, liners and steel target are meshed by Lagrangian algorithm with hourglass control. In order to improve the quality of the discrete elements, numerical models are discretized with 8-node hexahedral solid elements(SOLID164)[3,22]. For a circular liner in an axisymmetric EFP warhead, Fig.3(a) depicts the gridding results considered in our study. This approach provides elements that are approximately equally sized, but some asymmetries are introduced and some elements are not formed in a compact manner. In an effort to introduce more symmetry into the grid, it is possible to put uniform rings around the outer portions of the circle, as shown in the meshing process of liners. This provides the same number of elements in each of the

uniform rings. Here the asymmetries are reduced, but the elements get larger and larger as they move outward (for a constant radial increment)[4,22]. *BOUNDARY_SPC_SET[22] is used in the simulation model to restrict elements movement in the symmetrical boundaries. The symmetrical inhibit condition is added to the symmetrical surface of the model to restrict the node's displacement and rotation degrees of freedom. Contact may occur along the surfaces of a single body undergoing large deformation, between two or more deformable bodies, or between a deformable body and a rigid barrier. *CONTACT_SLIDING_ONLY_PENALTY[22] is used to model the impact between the dynamite and liner. The contact keyword between EFP and target is changed to *CONTACT_ERODING_SURFACE_TO_SURFACE. A large number of numerical calculation results prove that detonation products at about 30μs will no longer affect the characteristic parameters of EFP after the explosive is detonated. Therefore, the explosive is deleted at 30μs in the numerical calculation[21].

3.2 Material constitutive models and parameters

3.2.1 Material model for high explosive

High explosive (8701) are typically modeled by using the Jones-Wilkins-Lee (*JWL*) EOS, which models the pressure generated by chemical energy in an explosion. It can be written in the form

$$p = A_1\left(1 - \frac{\omega}{R_1 v}\right)e^{-R_1 v} + B_1\left(1 - \frac{\omega}{R_2 v}\right)e^{-R_2 v} + \frac{\omega e}{v} \tag{1}$$

Where p is the hydrostatic pressure; v is the specific volume, e is internal specific energy. The values of constants A_1, R_1, B_2, R_2, ω for many common explosives have been determined from dynamic experiments.

3.2.2 Material model for liners and steel target

To be able to describe the various phenomena taking place during contact explosion, it is necessary to characterize the behavior of materials under explosion-generated high strain rate loading conditions. Liners and target are both modeled by the Johnson-Cook (*J-C*) material model[23], which is suitable to model the strength behavior of materials subjected to large strains, high strain rates and high temperatures. The model defines the yield stress σ_y as

$$\sigma_y = \left[A + B\left(\overline{\varepsilon}^p\right)^n \right]\left[1 + C \ln \dot{\varepsilon}^* \right]\left[1 - \left(T^*\right)^m \right] \tag{2}$$

Where A, B, C, n and m are the material parameters determined by experiments. $\overline{\varepsilon}^p$ is the equivalent plastic strain, $\dot{\varepsilon}^* = \dot{\varepsilon}_p / \dot{\varepsilon}_0$ is the dimensionless effective strain rate at a reference strain rate $\dot{\varepsilon}_0 = 1s^{-1}$. T^* is the homologous temperature which is defined by $T^* = (T - T_{room})/(T_{melt} - T_{room})$, where T is the current temperature, T_{room} and T_{melt} are the room and melting temperatures, respectively.

Johnson and Cook[24] also developed a failure criterion that accounts for temperature, strain rate and strain path in addition to the triaxiality of the stress state. The model is based on damage accumulation, and has the basic form

$$D = \sum \frac{\Delta \varepsilon_y}{\varepsilon_f} \tag{3}$$

Where D is the damage to a material element, $\Delta\varepsilon_y$ is the increment of accumulated plastic strain, and ε_f is the accumulated plastic strain to failure under the current conditions of stress triaxiality, strain rate and temperature. Failure occurs when $D=1$, and in the finite element simulations, element erosion is used to remove elements that have reached the critical damage. The failure strain ε_f is defined as

$$\varepsilon_f = [D_1 + D_2 \exp D_3 \sigma^*][1 + D_4 \ln \dot{\varepsilon}^*][1 + D_5 T^*] \tag{4}$$

Where σ^* is the dimensionless pressure-stress ratio defined as $\sigma^* = \sigma_m / \overline{\sigma}$, σ_m is the mean stress normalized by the effective stress, $\overline{\sigma}$ is the effective stress, and D_1, D_2, D_3, D_4 and D_5 are the material parameters[24,25]. Details of finite

element modeling of 8701 explosive, liners and target are described in Table 1[21,24,25]. Considering the composition similarity of steel target, the parameters of #45 steel target[26] are used in the numerical simulation.

Table 1 Parameters of each material.

8701	ρ (g/cm^3)	D (km/s)	P_{CJ} (GPa)	A_1 (GPa)	B_1 (GPa)	R_1	R_2	ω	E_0 (GPa)	V_0
explosive	1.71	8.315	28.6	524.23	7.678	4.20	1.1	0.34	8.499	1.00
	ρ (g/cm^3)	G (GPa)	A(MPa)	B(MPa)	N	C	m	T_m	σ_s (GPa)	C (km/s)
Copper	8.97	46.50	90	292	0.31	0.025	1.09	1356	0.09	3.94
	S_1	S_2	S_3	γ_0	α	E_0	V_0			
	1.49	0	0	2.02	0.47	0	1.0			
	ρ (g/cm^3)	G (GPa)	A(MPa)	B(MPa)	N	C	m	T_m	σ_s (GPa)	C (km/s)
Iron	7.89	80	175	380	0.32	0.060	0.55	1811	0.09	3.57
	S_1	S_2	S_3	γ_0	α	E_0	V_0			
	1.92	0	0	2.02	0.47	0	1.0			
	ρ (g/cm^3)	G (GPa)	A(MPa)	B(MPa)	N	C	m	T_m	σ_s (GPa)	C (km/s)
Steel target	7.83	77	792	510	0.26	0.014	1.03	1793	0.09	4.57
	S_1	S_2	S_3	γ_0	α	E_0	V_0			
	1.49	0	0	2.17	0.46	0	1.0			

3.3 Formation process of EFP with different liner materials

The sequence of transforming a disc-shape liner into a slug is schematically shown in Table 2. The central portion of the liner moves relatively fast and developed into a 'head' section, whereas the other parts of the liner, travelling at relatively low speeds, lagged behind and formed the rear section of the slug. According to the fluid dynamics theory on penetration[27], to form a longer and stable penetrator, the liner material must be characterized by a high density, high acoustic velocity and high dynamic fracture elongation which can guarantee stretching of the penetrator. Due to the tensile strength and ductility of the copper is better than the material parameters of iron, the dimensionless ratio value of the length and diameter of copper EFP is approximately 2.6 while the dimensionless ratio value of the length and diameter of iron EFP is about 1.8 as the appearance of EFP is stable.

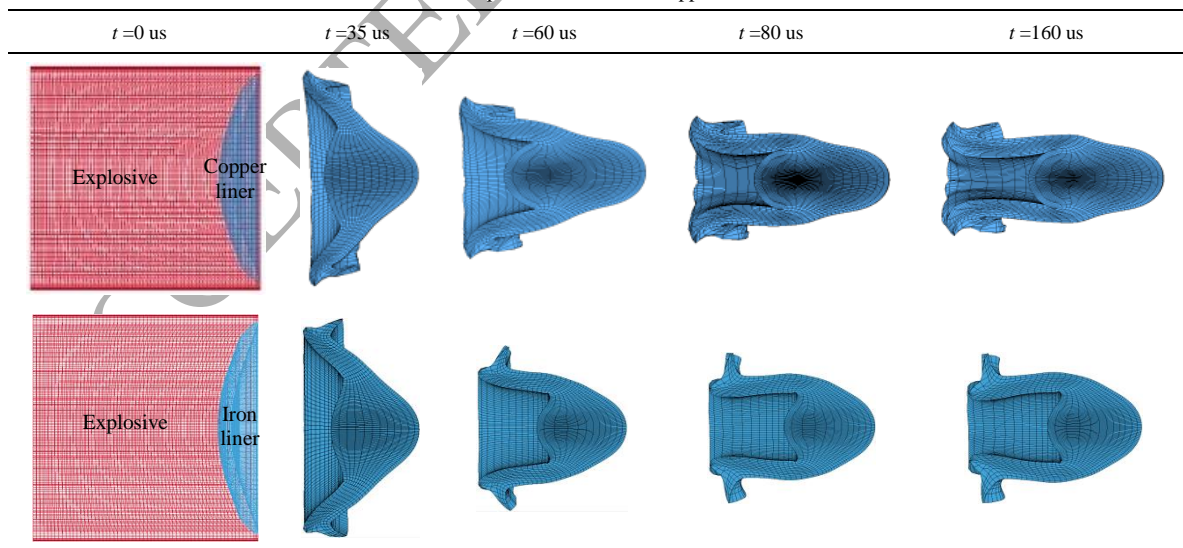**Table 2** Formation process of EFP with copper liner and iron liner.

Fig.4 displays velocity variation of EFPs with different liner material. According to the simulation results, the velocity of the copper EFP is about 1498.77m/s and the velocity of iron EFP is about 1649.33m/s. A comparison of the penetrator shapes and velocities shows that there is a slight velocity decrease for the copper EFP with a larger dimensionless ratio value of the length and diameter compared with iron EFP.
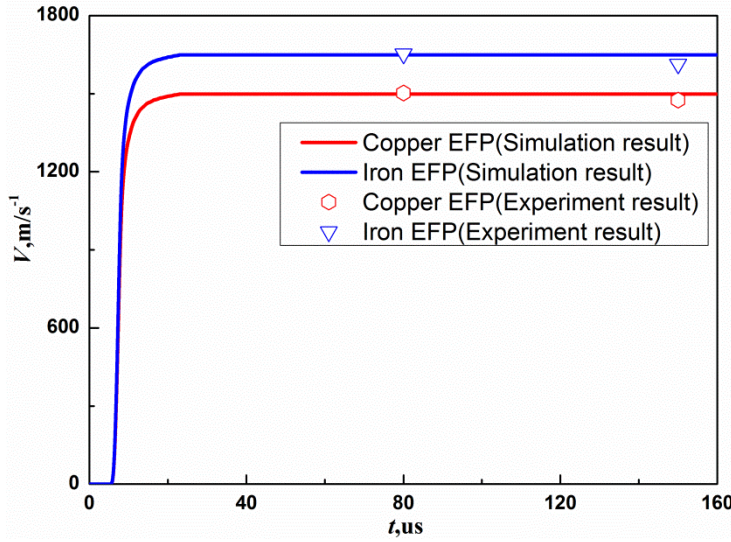
Fig.4. Velocity variations of EFP with different liner material.

4. Microstructure evolution of steel targets subjected to high velocity impact by EFP

4.1 Failure modes analysis of targets subjected to high velocity impact by EFP

High velocity impact caused by EFP will produce a sudden change of pressure between the projectile and target. In order to calculate the shock parameters of target impacted by EFP, the penetration is simplified as a normal and continuous process. That implies the direction of EFP movement is perpendicular to target surface and contact between EFP and target occurs simultaneously. Prior to impact, the EFP is travelling at velocity V, whereas the target is at rest. Upon impact, two compressive shock waves are created: one travels into the EFP, with velocity U_{p1} respect to a moving impact interface called Lagrangian referential and another travels into the target, with velocity U_{p2} (in the compressed region). The particle velocity in the compressed region of the EFP is reduced by a value U_p (the upward motion of the particles)so that the resultant particle velocity is V - U_{p1}. Thus

$$V - U_{P1} = U_{P2} \tag{5}$$

In order to determine the pressure, we make use of the equation for conservation of momentum.

For the copper EFP and steel target

$$P_1 = \rho_{01} U_{s1} U_{P1} \tag{6}$$

$$P_2 = \rho_{02} U_{s2} U_{P2} \tag{7}$$

The *EOS* state equation for the two materials are

$$U_{s1} = C_1 + S_1 U_{P1} \tag{8}$$

$$U_{s2} = C_2 + S_2 U_{P2} \tag{9}$$

Substituting Eqs.(8) and (9) into Eqs.(6) and (7) yields

$$P_1 = \rho_{01}(C_1 + S_1 U_{P1}) U_{P1} \tag{10}$$

$$P_2 = \rho_{02}(C_2 + S_2 U_{P2}) U_{P2} \tag{11}$$

Where ρ_{01} and ρ_{02} is the density of copper liner and steel target, V is the initial velocity of EFP, C_1, $S_1$and C_2, S_2 are the shock parameters of EFP and target, respectively.

There are two more requirements to establish the equations to predict the shock wave parameters of steel target: the material should be continuous across the impact interface and the pressure on the interface is the same($P_1=P_2$). Substituting Eq.(5) into Eq.(10), we can also obtain an equation with only one unknown parameter U_{P2}

$$P_1 = \rho_{01}C_1(V - U_{P2}) + \rho_{01}S_1(V - U_{P2})^2 \tag{12}$$

The shock wave parameters of target impacted by EFP can be calculated rapidly by a graphic solution, usually called the impedance matching technique[19]. Fig.5 illustrates the pressure-particle velocity curves for copper EFP and steel target during the high velocity impact. These curves are available for all materials whose *EOS* state equations are known. The *P-U* curves(I_{EFP} and T_{target}) for the different materials(copper and steel) can be determined on transparent papers according to Eqs.(10) and (11). To express Eq.(12) in the *P-U* plane, one has to make a change in coordinates. The origin is changed from 0 to *V* and the curve is inverted(the change of U_P to $-U_P$). This is indicated in Fig.5 by R_{EFP} which is the reflected shock wave in the projectile. By overlaying the direct curve(for the target T_{target}) with the inverted curve(for the projectile R_{EFP}) and setting its origin at *V*=1489m/s, one can easily finds their intersection point M(U_M, P_M). The pressure P_M is the initial parameter of impact pressure.
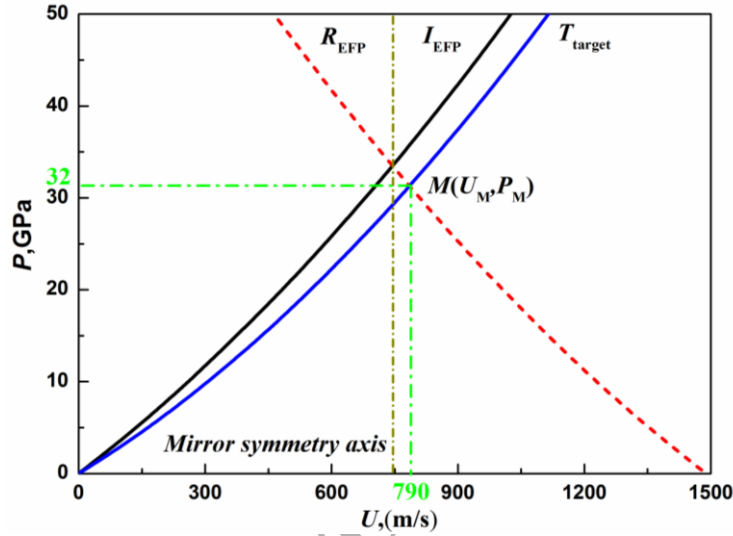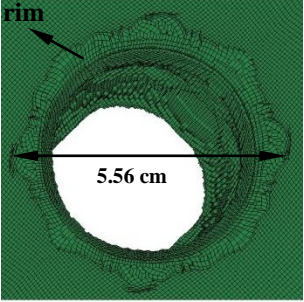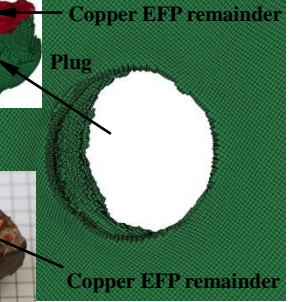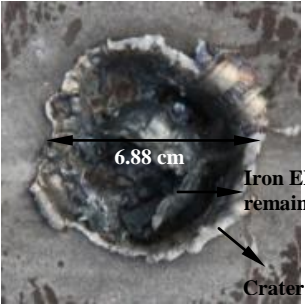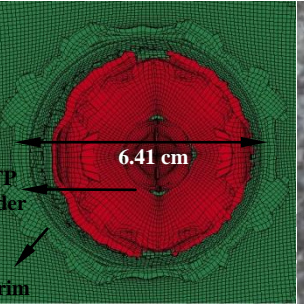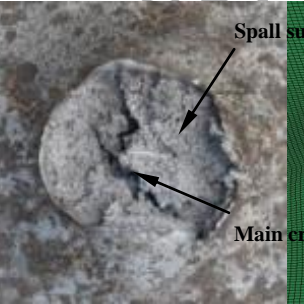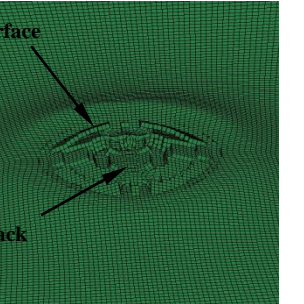

Fig.5. Graphic solution for high velocity impact of EFP (copper) on steel target.

A copper EFP, travelling at velocity of 1489 m/s, generates a shock wave pressure about 32GPa when it interacts with steel target in a mode in which there is concurrent deformation of both. Using the same calculation method, the collision pressure can reach as high as 36.44GPa when the steel target subjected to the high velocity (1632.73m/s) impact by iron EFP. As the pressure caused by high velocity impact of EFP at the deformation interface significantly exceeds the dynamic flow stress[19] ($P = 0.5\rho_{target}V_{EFP}^2$) of the steel target(8.6GPa and 10.4GPa), the crater formation process can be assumed to be guided by fluid dynamic.

According to Birkoff's[28] penetration theory about long cylinder into a metallic target, a plastic flow is produced transversely around the head of projectile when an EFP with a high velocity strikes on a finite target and the remainder of EFP will flow from the crater bottom to the crater rim as the penetration depth increases. The target material away from the interface between the target and EFP will stop this trend of flow. As a result, the material flows plastically along the crater wall to the free surface of the target, creating a jet that forms a rim above the target on the front surface. Subjected to high velocity impact by copper EFP, a series of dispersed and chip pieces of the superposition distribute on the crater rim and the average width of the entrance is 5.74cm in the experiment. For iron EFP, the crater rim seems to be integrally in a smooth flow state and the average width of the entrance is 6.88cm. This phenomenon is also proved to be matched very well with the corresponding simulation results, as shown at the entrance view in Table 3. As the penetration depth increases, the kinetic energy of EFP will be decreased due to the resistance of target through various energy absorbing mechanisms. At the end stage of penetration, the residual steel target is failure in the damage of plug under high velocity impact by the remainder of copper EFP. After the target has been perforated, the remainder of EFP and plug with reduced thickness and diameter are tightly integrated together and the residual velocity of plug is about 627.31 m/s measured in the experiment. Meanwhile, a series of irregular spall fragments are produced on the rear surface of the steel target since the energy of iron EFP cannot push out the plug of target, as shown at the exit view in Table 3.

Comparison between experimental and numerical results of target failure modes, residual EFP, plug and fragments are demonstrated in Table 3. On the one hand, it is observed that the dynamic response of steel targets change obviously subjected to high velocity impact of EFP with different liner material. On the other hand, simulation results related to terminal effects of copper and iron EFP have shown excellent agreement with experiment results and it also shows the reasonable of selected numerical models and accuracy of material parameters.

Table 3 Dynamic response of the finite steel targets subjected to high velocity impact by copper and iron liner EFP.

	Entrance view		Exit view	
	Experimental results	Simulation results	Experimental results	Simulation results

The copper EFP striking the steel target effectively distributes its initial kinetic energy between itself as a deforming and eroding body, and the deforming and eroding target, as well as the energy required to separate a plug from the rear of a target with finite thickness. The energy required for plug separation or break-out from the target is proportional to the plug diameter, the target material shear strength, and the square of the target thickness[12,13]. The energy derives from the projectile kinetic energy and is localized at the projectile circumference where the shear bands ultimately form a cylindrical, solid-state flow zone[29] allowing the plug volume to be pushed out of the target[30,31]. A layer of copper covers on the surface of crater wall. The layer thickness of copper, which displays an extreme plastic flow, shows a gradient tendency from 2mm close to the crater bottom to 0.5mm close to the crater rim, as illustrated in Fig.6(b). In the crater wall, there is an interface with a thickness about 1.5µm and the copper material of EFP impregnates into the matrix of steel target. This feature can be observed from the line scanning views of cross-sectional elemental distribution of copper and iron, as shown in Fig.6(c). The steel target fails in the mode of spall under high velocity impact by iron EFP. Spall is a dynamic material failure process that occurs during the propagation process of release wave reflected from the rear surface of steel target[32]. If the release wave is of sufficient magnitude, the tensile stress formed by the interaction of release wave and the unloading section of initial shock wave will exceed the tensile yield limit(σ^*) of target material and the spall occurs. Otherwise, the process of spall will be generated at the interaction(collision) position of two release waves, produced by the incident, unloading wave propagating from the rear surface of the projectile and by the release wave due to the reflection of the compression wave from the rear surface of the target[33]. In our study, the release wave from the rear surface of the target is about 36.44GPa(the value is approximately equal to the collision pressure caused by the high velocity impact of EFP), and the intensity of this release wave is far greater than tensile yield limit($\sigma^* = 2.45$GPa)[34] of target during the spall failure mode. Thus, a series of irregular spall fragments are produced on the rear surface of the steel target, as shown in Fig.6(d). The iron element in the crater wall of steel target is mainly derived from two parts, including iron liner and matrix of steel target, as shown in
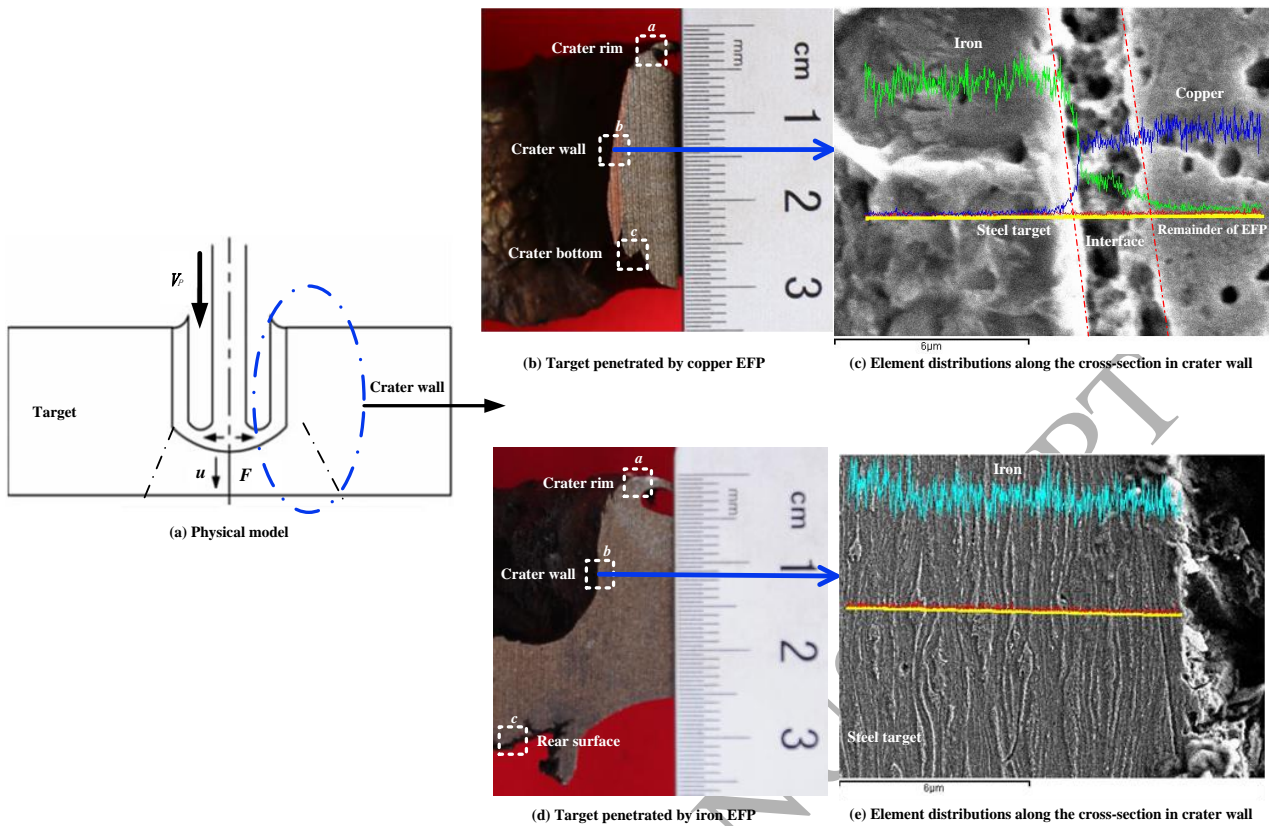
Fig.6(e).

(a) Physical model

(b) Target penetrated by copper EFP

(c) Element distributions along the cross-section in crater wall

(d) Target penetrated by iron EFP

(e) Element distributions along the cross-section in crater wall

Fig. 6. Failure modes of steel targets subjected to high velocity impact by copper and iron EFP.

4.2 Morphology analysis of steel targets

Fracture is often the culmination of continued deformation. Therefore, fracture surfaces may retain manifestations of the deformation that the material is subjected to. The dynamic process of fracture behavior of steel target under high velocity impact by EFP can be inferred from the microstructure evolution of fracture morphology at different positions of the crater.

The surface material of steel target experiences severe plastic deformation subjected to impact at a certain angle to the movement direction of EFP, creating crater rim due to over-extrusion. In this mode of failure, a considerable incompletely elongated dimples are spread evenly on the crater rim, indicating that the material of crater rim fails due to shear stress, as shown in Table 4(crater rim). The deep and dense dimples formed by penetration of copper EFP appear on the crater rim and elongated and irregular dimples formed by penetration of iron EFP take an advantage distribution on the crater rim. Observing the fracture morphology of fracture surfaces on the crater wall, plenty of parabolic dimples are distributed on the surface of copper EFP remainder plated to the crater wall while incompletely elongated dimples and slightly equiaxed dimples formed by penetration of iron EFP are both observed from the morphology of fracture surface of crater wall, as shown in Table 4(crater bottom).

On the rear surface of the steel target penetrated by copper EFP, Failures (such as micro-cracks, micro-voids, and micro-debris) initiate where the tensile stress exceeds the tensile yield limit of the target, as shown in Table 4(Rear surface). Under high velocity impact by iron EFP, the material on the rear surface of target fails mainly along the cleavage plane which is a low-energy fracture that propagates along the well-defined low-index crystallographic plane. A cleavage fracture has perfectly matching faces and is completely flat and featureless. The steel target mainly consists of polycrystalline metal and contains grain boundaries, dislocations and other imperfections that affect the propagating cleavage fracture. The microstructure evolution of rear surface indicates that steel target exhibits excellent brittle features under strong impact, and the spall fracture behavior appears possibly a behavior of brittle tearing.

Table 4 Morphology features of fracture surfaces in the failure modes of plug and spall.

	Copper EFP	Iron EFP
Crater rim		
Crater wall		
Crater bottom		
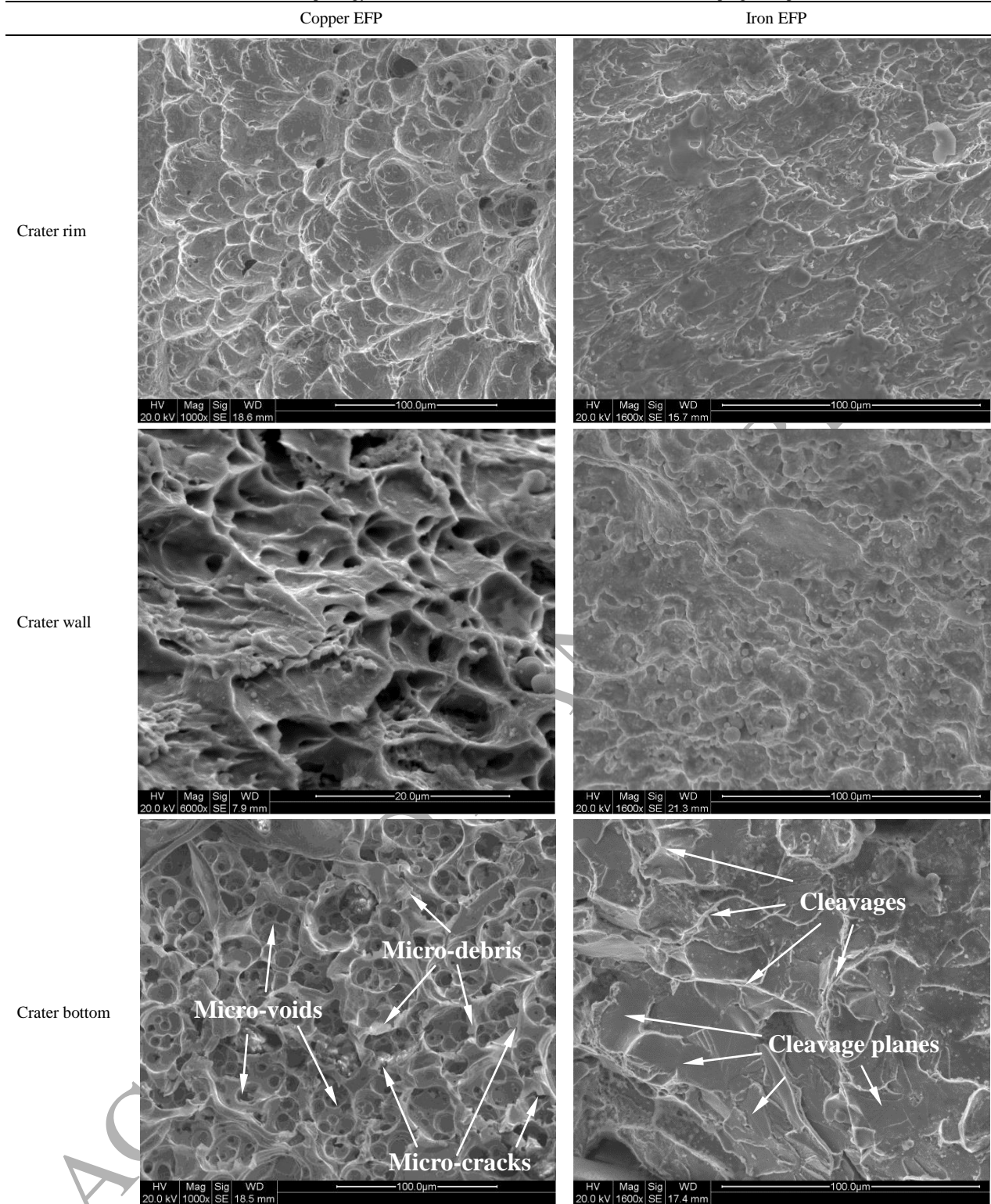
4.3 Microstructure evolution of steel target for high velocity impact crater

The structure change of solid is governed by external factors such as pressure and temperature and internal factors such as composition and internal stresses due to defects(dislocations, point defects, interface)[35]. High velocity impact caused by EFP produces sudden changes of pressure that may result in polymorphic transformations and microstructural evolutions of the steel target[36,37].

The finite thickness steel target subjected to impact loading of copper EFP fails in the damage mode of plug, as shown in Fig.7(a-1). Investigation of the mechanism by which materials respond to dynamic extremes, including high strains and high strain rates resulting from plug failure mode is of paramount importance in understanding the dynamic process of plug

fracture behavior[38]. The most widely used physical models of plug based on localized shear deformation or so-called shear instabilities forming narrow bands of dynamically recrystallized nano-grain structures have been studied for many years[39,40]. Although such localization can manifest itself in narrow, isolated, and repetitious bands, the features are always associated with extreme deformations characterized by very high strains and strain rates which result in some form of material flow state accommodated by dynamic recrystallization (DRX)[41,42]. In our study, a typical microstructural change in the shallow surface of the crater wall is the narrow zone of dynamically recrystallized material(including the layer of copper plated to the steel crater wall and a little part of steel target) extending from the free surface of the crater. In the zone of DRX, the microstructures of the completely dynamic recrystallised grains appear. The whole part of copper plated to the crater wall surface undergoes completely dynamic recrystallization, and the average size of the refined grains significantly decreases to approximately 10μm. The dynamic recrystallization materials of steel target adjacent to the copper-iron interface of crater wall show a state of superplastic flow[31], and the general flow-like features of the microstructure suggest extremely plastic deformation from the crater floor upward to the rim area. The thickness of this flow-like zone paralleling to the crater wall is about 21.3 μm, as shown in Fig.7(a-2).
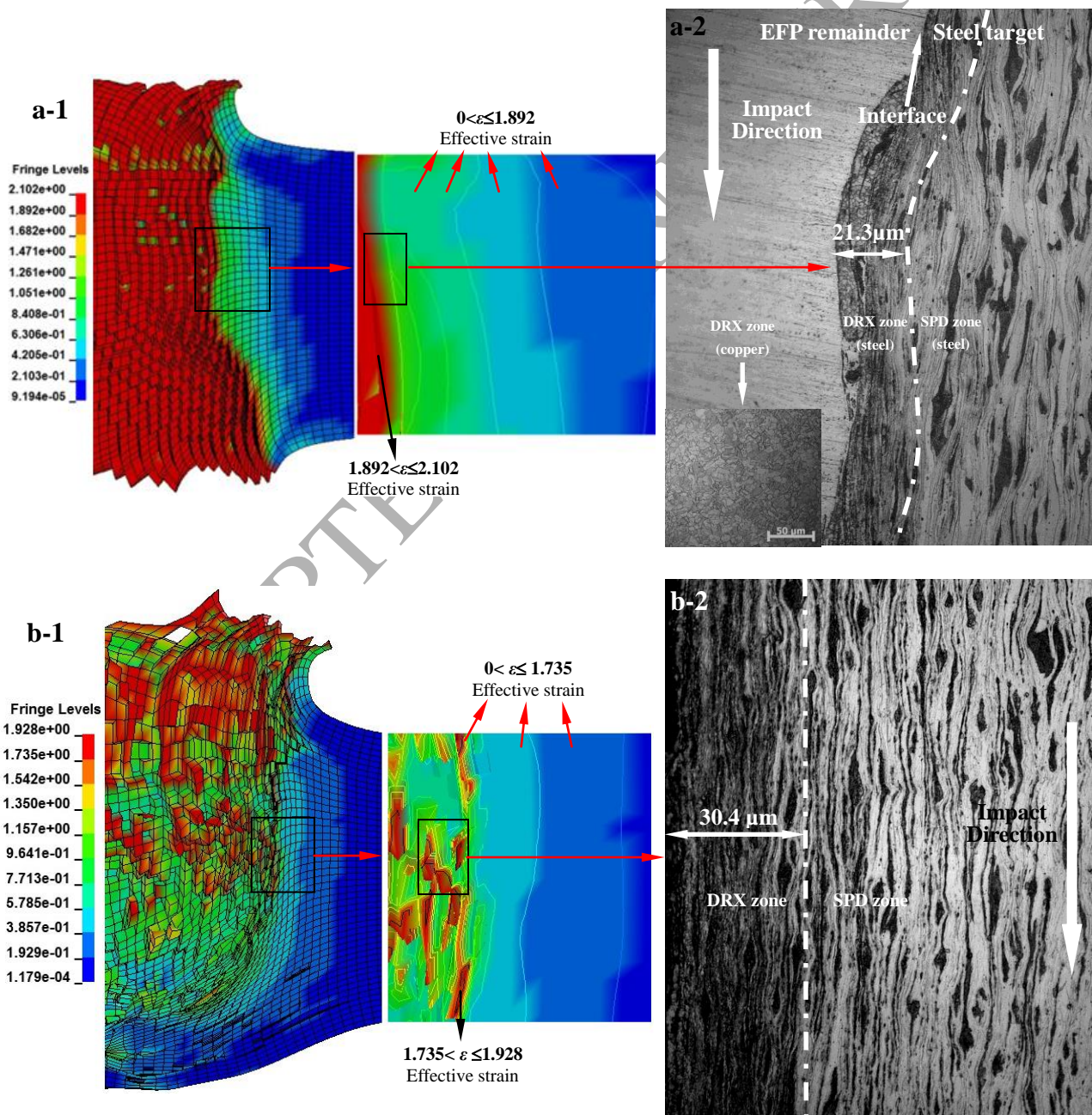

Fig. 7. Crater-related microstructures of steel targets subjected to high velocity impact by copper(a) and iron(b) EFP.

Corresponding numerical simulation results about high velocity impact crater of copper EFP indicates that the maximum effective strain ε can reach as high as 2.102 plated to the crater wall. And the effective strain begins to drop rapidly as the position away from the crater wall. Considering the dynamic recrystallization process and extremely plastic deformation in the zone of this area, the high plastic strain can fully accommodate the grains deformation of steel target during these dynamic process. Therefore, the maximum rate of plastic strain can reach as high as 4.2×10^4 s^{-1} since the process of penetration can be completed in 50μs as shown in the simulation process[1]. Subjected to high velocity impact by iron EFP, the steel target fails in the mode of spall and numerical simulation results indicates that the maximum effective strain plated to the crater wall is 1.928, which is slight lower than the maximum effective strain caused by copper EFP, as illustrated in Fig.7(b-1). A plot of localized deformation mainly locates on the crater wall indicates that the most extremely plastic deformation is concentrated within the dynamic recrystallization zone. Compared with the microstructure evolution of steel target subjected to high velocity impact by copper EFP, a layer of iron EFP remainder together with DRX refined grains of steel target covers on the surface of crater wall when the finite steel target penetrated by iron EFP, as depicted in Fig.7(b-2). Therefore, the thickness of irregular DRX zone(30.4μm) formed by the interaction between iron EFP and steel target is wider than the thickness of DRX zone formed by the penetration of copper EFP. Marchand and Duffy[43]give the relationship between the width of the DRX zone and the strain within the zone. Molinari and Clifton[44]consider different thermoviscoplastic flow laws to determine the conditions for localization during simple shear, as well as the profiles of the local strain and strain rate within an initial geometrical defect during the global deformation process. A common result of these analyses is that during plastic deformation, the global plastic deformation is then concentrated within the extremely plastic strain zone which experiences dynamic recrystallization.
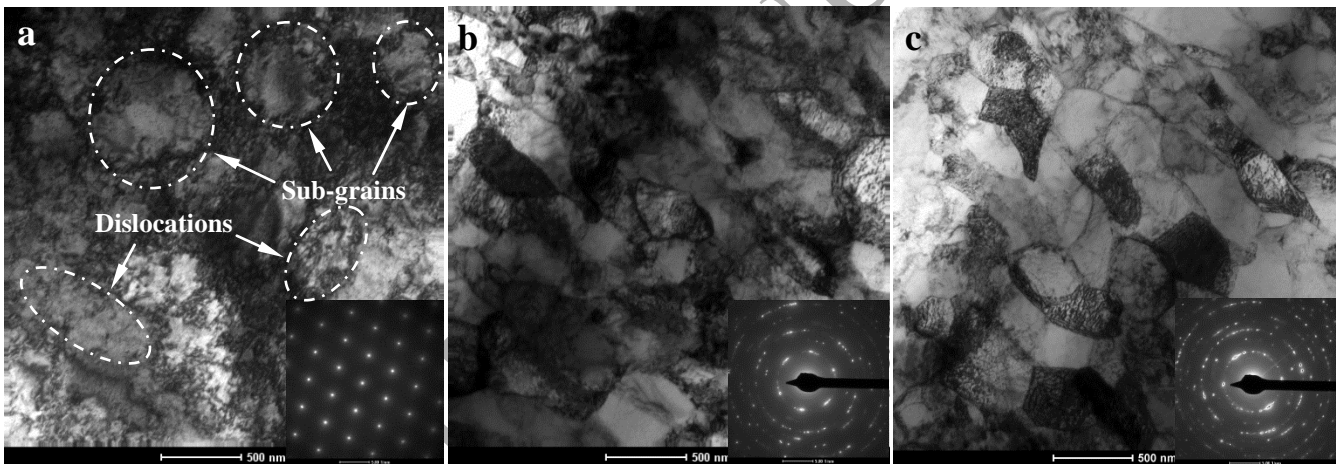

Fig. 8. TEM images of the well refined DRX grains. (a) Sub-grains with dislocations and a corresponding SAED pattern of copper EFP remainder, (b) Well refined DRX grains and a corresponding SAED pattern of steel target(copper EFP), (c) Well refined DRX grains and a corresponding SAED pattern of steel target (iron EFP).

Plastic deformation by dislocation and twinning are considered as competitive mechanisms for metal materials. Given that no twins or elongated sub-grains are observed in DRX zone of copper EFP remainder, dislocation movements should be the predominant mechanism that governs DRX process in the crater wall. Fig. 8(a) shows TEM image of DRX grains that dislocation gliding facilitates grain refinement in the DRX process and a corresponding selected-area electron diffraction(SAED) pattern of microstructures. In this condition, increased dislocation density is a warranty for extremely plastic deformation, and the dislocation drag controlled plasticity is the only possible mechanism. These fragmented sub-grains eventually form small, recrystallized grains, which help in the further flow of the material[45]. Figs. 8(b) and (c) provide evidence that the well refined DRX grains with clear grain boundaries in the centre of DRX zone of steel target. The initial steel target grain size of roughly 53.17 μm(as shown in Fig. 9) has been refined to the size in nanometer level. On the average, the grain sizes in the centre of DRX zone are less than 200nm(as shown in Figs. 8(b) and (c)). The refined substructures are generated by shock loading depending on a number of shock wave parameters and the pressure is also the most important one[46]. Under high velocity impact of copper and iron EFP, the shock wave pressure can reach as high as

32GPa and 36.44GPa, respectively. Since the iron EFP will generated a more higher collision pressure than copper EFP during the penetration process of the finite steel target, the DRX grains in Fig. 8(c)(iron EFP) have been refined smaller than the DRX grains in Fig.8(b)(copper EFP). These microstructural features are more significant in magnified strips compared with the corresponding SAED patterns of refined grains in different DRX zones. In summary, the grains in matrix of steel target start fragmenting, recombination and growing under high velocity impact by EFP and the well refined grains play a key role in this dynamic process.

From crater wall to the matrix of steel target, the grains experience severe plastic deformations which is mainly composed of DRX grains, heavily elongated grains and distorted grains with different grain sizes, as depicted in Fig.9. An severe plastic deformation (SPD) zone characterized by heavily deformed and distorted polycrystalline material is also found below the DRX zone in the steel target. Given the transverse movement of target material squeezed by EFP in the crater wall, the grains are elongated along the impact axis under high strain-rate deformation. The material in SPD zone shows extreme plastic deformation evolved into a less severely distorted grain structure (plastic deformation zone). In the wide zone of plastic deformation zone, grains show a relatively clear boundaries. From the free surface of crater wall to the interface between copper and steel target, the microhardness has a slight increase from 64Hv to 86Hv in the layer of copper plated to the crater wall. The maximum microhardness is observed on the interface between DRX and SPD zones in the steel target. In the DRX zone, the grains grow and re-combine and the microhardness in this zone slightly decreases. The maximum microhardness(302 Hv) of steel target subjected to high velocity impact by copper EFP is higher than the maximum microhardness(275 Hv) of steel target subjected to high velocity impact by iron EFP. Severe plastic deformations in SPD zone cause irreversible damage to the target, and the microhardness is improved significantly. External shocks acting on the material in the SPD zone play an important role in material hardening.
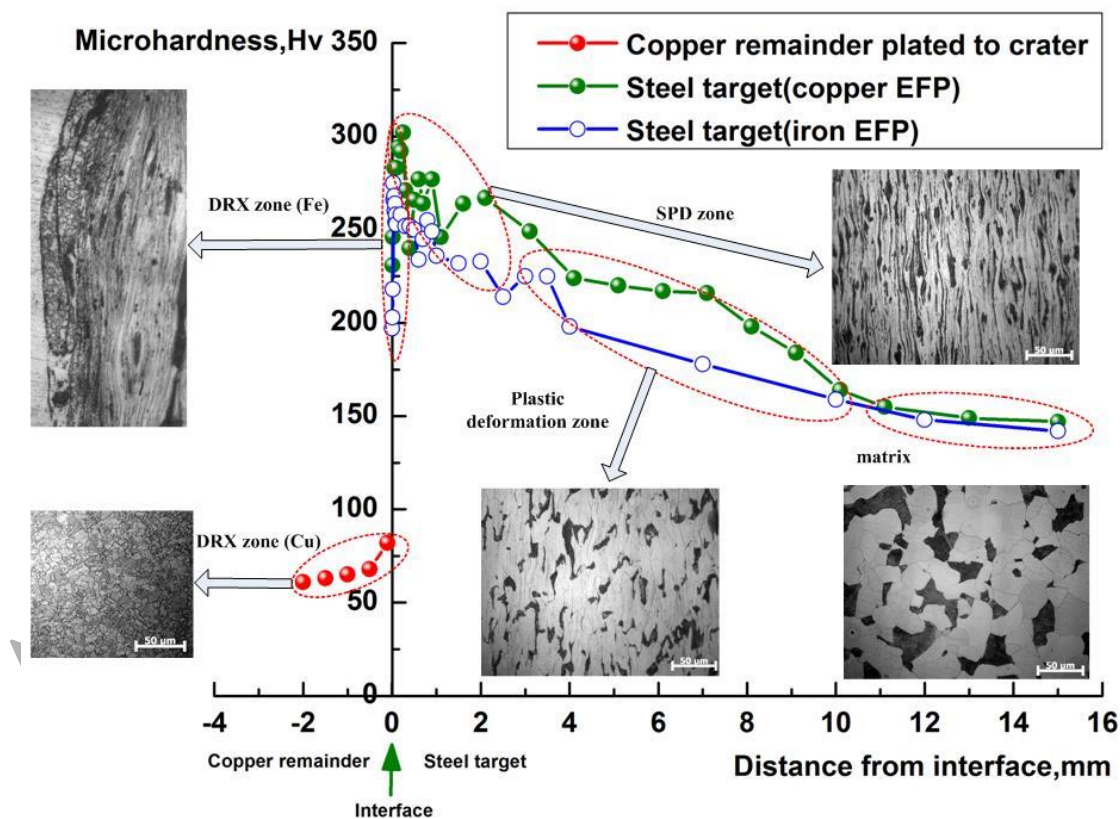

Fig. 9. Microhardness profile extending from the crater wall to the matrix of targets.

5. Conclusions

In this work, terminal effects of the finite steel targets subjected to high velocity impact by copper and iron liner EFP are compared from a macro perspective. Correspondingly, morphology features of fracture surface and microstructure evolution

of the steel targets are investigated in detail. The major conclusions are as follows:

1. The finite steel targets experience the failure modes of plug and spall subjected to high velocity impact by copper and iron liner EFP warheads with the same shaped charge structure. A copper EFP can effectively break down the finite steel target with a thickness of 2cm and the maximum penetration depth of iron liner EFP is less than half penetration depth of copper liner EFP.

2. The collision pressure(36.44GPa) generated by high velocity impact of iron EFP is higher than the collision pressure(32GPa) of copper EFP. The whole part of copper EFP remainder and partial material of steel target undergoes completely dynamic recrystallization. The thickness of irregular DRX zone(30.4μm) formed by the interaction between iron EFP and steel target is wider than the thickness of DRX zone(21.3μm) formed by the penetration of copper EFP.

3. Morphology analysis of fracture surfaces indicates that the copper EFP remainder shows extremely plastic deformation which consists of elongated parabolic dimples in the crater wall and the mild carbon steel target exhibits excellent brittle features that material fails mainly along the cleavage facets on the rear surface of target under strong impact of EFP.

4. Numerical simulation results indicate that the highest plastic strains at the crater wall can reach about 2 which can fully accommodate the grains deformation of steel target during the dynamic recrystallization process at strain rates of the order of 10^4 s^{-1}, and the average size of the refined DRX grains significantly decreases from 53.17 μm to approximately 200 nm.

Acknowledgments

References

1 Wu, J., Liu, J. B. and Du Y. X. (2007) Experimental and numerical study on the flight and penetration properties of explosively-formed projectile. *Int. J. Impact Eng.*, **34**, 1147-1162.

2 Yu, C., Tong, Y. J., Yan, C. L., Li, F. B., Gui, Y. L., Zhang, M., Wang, B. R., Xie, P. H. and Li L. Z. (1999) Applied research of shaped charge technology. *Int. J. Impact Eng.*, **23**, 981-988.

3 Johnson, G.R. and Stryk, R.A. (2006) Some considerations for 3D EFP computations. *Int. J. Impact Eng.*, **32**, 1621-1634.

4 Cardoso, D. and Teixeira-Dias, F. (2016) Modelling the formation of explosively formed projectiles(EFP). *Int. J. Impact Eng.*, **93**, 116-127.

5 Weickert, C.A. and Gallagher, P.J. (1993) Penetration of explosively formed projectiles. *Int. J. Impact Eng.*, **14**, 809-818.

6 Rabczuk T, Areias P, Belytschko T. (2010) A meshfree thin shell method for nonlinear dynamic fracture. *Int. J. Numer. Meth. Eng.*, **72(5)**,524–548.

7 Rabczuk, T., Gracie, R., Song, J.H. and Belytschko, T. (2010) Immersed Particle Method for Fluid-Structure Interaction. *Int. J. Numer. Meth. Eng.*, **81**,48-71.

8 Rabczuk T, Areias P, Belytschko T.(2007) A simplied meshfree method for shear bands with cohesive surfaces. *Int. J. Numer. Meth. Eng.*, **69(5)**,993–1021.

9 Sui, S. and Wang, S. (2000) *Terminal effects*, Weapon Industry: Beijing.

10 Murr, L. E., Garcia, E. P., Ferreyra, E. T., Niou, C. S., Rivas, J. M. and Quinones, S. A. (1996) Microstructural aspects of hypervelocity impact cratering and jetting in copper. *J. Mater. Sci*., **31**, 5915-5932.

11 Murr, L. E., Trillo, E. A., Pappu, S. and Kennedy, C. (2002) Adiabatic shear bands and examples of their role in severe plastic deformation. *J. Mater. Sci.*, **37**, 3337-3360.

12 Staudhammer, K. P., Murr, L. E., and Meyers, M. (2001) *Fundamental Issues and Applications of Shock Wave and High-Strain-Rate Phenomena*, A. (Eds.), Elsevier Science: Amsterdam.

13 Martinez, F., Murr, L.E., Ramirez, A., Lopez, M.I. and Gaytan, S.M. (2007) Dynamic deformation and adiabatic shear microstructures associated with ballistic plug formation and fracture in Ti-6A1-4V targets. *Mater. Sci. Eng. A.*, **454**, 581-589.

14 Ren, B. and Li, S. (2010) Meshfree simulations of plugging failures in high-speed impacts. *Comput. Struct.*, **88 (15),** 909-923.

15 Pappu, S. and Murr, L. E. (2002) Hydrocode and microstructural analysis of explosively formed penetrators. *J. Mater Sci.*, **37**, 233-48.

16 Murr, L. E., Pappu, S., Kennedy, C., Niou, C-S. and Meyers M. A. (1996) Tantalum Microstructures for High-Strain-Rate Deformation: Shock Loading, Shaped Charges and Explosively Formed Penetrators. I*n: Tantalum Symposium, TMS Annual Meeting,* Anaheim, CA, 145-155.

17 Murr, L. E., Meyers, M. A., C. S., Niou, Y. J., Chen, S., Pappu and C. Kennedy. (1997) Shock-induced deformation twinning in tantalum. *Acta Mater*, **45**, 157-175.

18 Pappu, S(2000). Hydrocode and microstructural analysis of explosively formed penetrators. PhD Thesis; The University of Texas At El Paso: 2000.

19 Meyers, M. A.(1994) Dynamic Behavior of Materials, 1st ed, John Wiley & Sons: New York.

20 Zhao, C. X., Qian, F., Zhang, H. Z., Ji, C., Lv, Y. and Xie, Q. M. (2015) Influence of liner material on formation of multiple explosively formed projectiles warhead parameters. *Advanced Materials Research*, **1096**, 37-41.

21 Li, W. B., Wang, X. M. and Li, W. B. (2010) The effect of annular mufti-pout initiation on the formation and penetration of an explosively formed penetrator. *Int. J. Impact Eng.*, **37**, 414-424.

22 Hallquist J.O. (1997). LS-DYNA Theoretical Manual, Livermore Software Technology Corporation, Livermore, CA, USA.

23 Johnson C.R., Cook W.H. (1983). A constitutive model and data for metals subjected to large strain, high strain rates and high temperature. In. Proceedings of the 7th International Symposium on Ballistics, Hague, Netherlands:541-548.

24 Johnson GR, Cook WH. (1985). Fracture characteristics of three metals subjected to various strains, strain rates, temperatures and pressures. *Engineering Fracture Mechanics*, **21**:31–48.

25 Chen G., Chen Z.F., Xu W.F., et al. (2007). Investigation on the *J-C* ductile fracture parameters of 45 steel. *Explosive and Shock Waves* **27**:131-135.

26 Li, Z.C., Zhu, Z.P. and Xue, J.F. (1995). *Steel Materials Handbook*, China Materials Resource Publication,12.

27 Eighth Department of Beijing Institute of Industry. (1979) *Explosive and Its Application*, National Defense Industry Press: Beijing.

28 Birkhoff, G., MacDougall, D.P., Pugh, E. M. and Taylor, G. I. (1948) Explosives with Lined Cavities. *J. Appl. Phys.*, **19**, 563-582.

29 Ren, B., Qian, J., Zeng, X., Jha, A. K., Xiao, S. and Li, S. (2011) Recent developments on thermo-mechanical simulations of ductile failure by meshfree method. *Comput. Method. Appl. M*., **200 (5)**, 797-811.

30 Gonzalez, B., Murr, L. E., Valerio, O. L., Esquivel, E. V. and Lopez, H. (2003) Microbands and microtwins associated with impact craters in copper and

brass targets: the role of stacking fault energy. *Mater. Charact.*, **49**, 359-366.

31 Li, J. C. M. and Yang, F. (2003) Growth of denuded zone by grain boundary fluid flow in Mg alloys. *Scripta Materialia.*, **48**, 991-995.

32 Curran, D. R., Seaman, L. and Shockey, D. A. (1987) Dynamic failure of solids. *Phys Rep*., **147**, 253-388.

33 Ren, B. and Li, S. (2012) A three-dimensional atomistic-based process zone model simulation of fragmentation in polycrystalline solids. *Int. J. Numer. Meth. Eng.*, **93 (9)**, 989-1014.

34 Sun., C. W. (2011) *Explosive physics*, Science Press: Beijing.

35 Antoun, T. (2003) *Spall Fracture*, Springer Science & Business Media: New York.

36 Murr, L. E., Trillo, E. A., Bujanda, A. A. and Martinez, N. E. (2002) Comparison of residual microstructures associated with impact craters in fcc stainless steel and bcc iron targets: the microtwin versus microband issue. *Acta Mater.*, **50**, 121-131.

37 Murr, L. E. and Esquivel, E. V. (2004) Review observations of common microstructural issues associated with dynamic deformation phenomena: Twins, microbands, grain size effects, shear bands, and dynamic recrystallization. *J. Mater. Sci.*, **39**, 1153-1168.

38 Murr, L. E., Ramirez, A. C., Gaytan, S. M., Lopez, M. I., Martinez, E. Y., Hernandez, D. H. and Martinez, E. (2009) Microstructure evolution associated with adiabatic shear bands and shear band failure in ballistic plug formation in Ti-6Al-4V targets. *Mater. Sci. Eng. A.*, **516**, 205-216.

39 Zener, C. and Hollomon, J. H. (1944) Effect of strain rate upon plastic flow of steel. *J. Appl. Phys.*,**15**, 22-32.

40 Xu, Y. B., Bai, Y. L. and Meyers, M.A. (2006) Deformation, phase transformation and recrystallization in the shear bands induced by high-strain rate loading in titanium and its alloys. *J. Mater.Sci. Technol.*, **22**, 737-746.

41 Langdon, T. G. (2009) Seventy-five years of superplasticity: historic developments and new opportunities. *J. Mater. Sci.*, **44**, 5998-6010.

42 Rivas, J. M., Quinones, S. A. and Murr, L. E. (1995) Hypervelocity impact cratering: microstructural characterization. *Scripta Metall Mater*., **33**, 101-107.

43 Marchand, A. and Duffy, J. (1988) An experimental study of the formation process of adiabatic shear bands in a structural steel. *J. Mech. Phys. Solids.*, **36**, 25l-283.

44 Molinari, A. and Clifton, R. (1987) Analytical characterization of shear localization in thermoviscoplastic materials. *J Appl Mech.*, **54**, 806-812.

45 Guo, W., Li, S.K., Wang, F.C. and Wang, M. (2009) Dynamic recrystallization of tungsten in a shaped charge liner. *Scr. Mater*., **60**, 329-332.

46 Chen, H (2012). Research on dynamic deformation in process of jet formation and penetration. PhD Thesis; Nanjing University of Science & Technology: March 2012.